

Optimizing electrode positions for 2D Electrical Impedance Tomography sensors using deep learning

Danny Smyl^{a,b}, Dong Liu^{c,d,e}

^a*Department of Civil and Structural Engineering, University of Sheffield, Sheffield, UK*

^b*The Integrated Civil and Infrastructure Research Centre (ICAIR), Sheffield, UK*

^c*Hefei National Laboratory for Physical Sciences at the Microscale and Department of Modern Physics, University of Science and Technology of China, Hefei 230026, China*

^d*CAS Key Laboratory of Microscale Magnetic Resonance, University of Science and Technology of China, Hefei 230026, China*

^e*Synergetic Innovation Center of Quantum Information and Quantum Physics, University of Science and Technology of China, Hefei 230026, China*

Abstract

Electrical Impedance Tomography (EIT) is a powerful tool for non-destructive evaluation, state estimation, process tomography, and much more. For these applications, and in order to reliably reconstruct images of a given process using EIT, we must obtain high-quality voltage measurements from the EIT sensor (or structure) of interest. Inasmuch, it is no surprise that the locations of electrodes used for measuring plays a key role in this task. Yet, to date, methods for optimally placing electrodes either require knowledge on the EIT target (which is, in practice, never fully known), are computationally difficult to implement numerically, or require electrode segmentation. In this paper, we circumvent these challenges and present a straightforward deep learning based approach for optimizing electrodes positions. It is found that the optimized electrode positions outperformed “standard” uniformly-distributed electrode layouts in all test cases using a metric independent from the optimization parameters.

Keywords: Electrical impedance tomography, inverse problems, nondestructive evaluation

1. Introduction

In Electrical Impedance Tomography (EIT), the aim is to reconstruct a conductivity distribution inside an object using boundary measurements. Information gained from the reconstructed conductivity is useful in a number of engineering applications, such as damage detection [1, 2] and stress/strain localization [3, 4] in composites, crack detection using conductive sensors [5, 6], process tomography [7], and more. Owing to increases in computational resources and knowledge transfer on EIT imaging methods (e.g. the EIDORS project [8]), the use of EIT in industrial applications has dramatically increased over the past 20 years.

We are certainly inspired by the recent advances and increased usage of EIT; however, there remain significant challenges in EIT imaging making it difficult to reliably apply in many engineering applications. The first is challenge is fundamental to EIT – its generally low spatial resolution resulting from the diffusive nature of electric fields. The second challenge is the sensitivity of the conductivity on the boundary measurements, which results from the severely ill-posed and nonlinear EIT inverse problem [9]. Assuming a fixed target, i.e. we can not reasonably change the geometry or constitution of the target, our best *physical* options for mitigating the second challenge is to optimize the current injection and/or electrode configuration. While the former is well addressed in the literature [10, 11], regimes for optimizing electrode positions are scarce. Perhaps the most relevant works addressing large degree of freedom systems common in engineering applications include an electrode segmentation system [12] and elegant optimization regimes which may (i) require prior knowledge on the target conductivity distribution or (ii) be computationally demanding or difficult for new users to implement [13, 14].

In this work, we circumvent the need to segment electrodes and implement complicated optimization algorithms with limitations (i) and (ii). To do this, we present a straightforward and fast deep learning-based approach for electrode position optimization which aims to minimize the ill-conditioning of the EIT Hessian matrix and the fit between the least-squares solution and true (training) distribution. We begin this paper by providing motivation for the optimization problem and outline the electrode position optimization algorithm. Following, we provide representative demonstrations of optimized electrode configurations using different geometries and derive a metric independent from the optimization parameters to evaluate sensor quality. We

Email addresses: d.smyl@sheffield.ac.uk (Danny Smyl), dong2016@ustc.edu.cn (Dong Liu)

then use this metric to illustrate potential improvements in using optimized electrode positioning relative to “standard” electrode positions. Lastly, discussion and conclusions are presented.

2. Optimizing electrode positions using deep learning

We begin this section by first describing the purpose of optimizing electrode positions in EIT. Following, we outline the proposed deep learning based optimization approach and the motivation for selecting training parameters. Lastly, we detail the electrode position optimization algorithm and practical aspects on implementation.

2.1. Background, nonlinearity, ill-conditioning, and ill-posedness

The purposes of optimizing electrode positions are to (a) maximize the quality of information contained in EIT measurements, (b) improve the conditioning of the EIT inverse problem, and (c) ultimately improve the reliability of EIT measurements and quality of reconstructions. As a whole, accomplishing (a) - (c) will improve the robustness and quantitative nature of EIT information used for engineering and physical science applications – which is the primary motivation for this article. In this subsection, we will discuss and derive key variables including information from points (a) - (c) to drive training for the electrode position optimization algorithm described in the next subsection.

The initial challenge arising in electrode position optimization stems from the realization that the EIT forward problem, computing boundary voltage measurements V from conductivity σ , is a nonlinear problem [9]. In this work, the nonlinearity is numerically manifested via the the finite element version of the complete electrode model [15]. If we write down the so-called ‘noiseless observation model’

$$V = U(\sigma) \quad (1)$$

we immediately observe that solving the EIT inverse problem, estimating σ from V , is highly dependent on the properties of this numerical forward model, U . Importantly, the nonlinearity of U results in a severely ill-conditioned sensitivity matrix $J = \frac{\partial U(\sigma)}{\partial \sigma}$ and Hessian approximation $H = J^T J$ [16]. In particular, the ill-conditioning of H has a large impact on the ill-posedness of least-squares based solutions to the EIT reconstruction problem, which is usually addressed using regularization techniques. However, we can also reduce the ill-conditioning of H to mitigate ill-posedness by reducing the Hessian’s condition number κ , where $\kappa(H) = \|H^{-1}\| \|H\|$ is a scalar value. Practically speaking, reducing $\kappa(H)$ lowers the sensitivity of outputs computed using H on the small changes to input values – in this case the sensitivity of σ to small changes in V . Based on these reasons, the selection of $\kappa(H)$ as the first input parameter used in training the optimization algorithm is a clear choice and addresses points (b) and (c).

The choice of a second input parameter, required to address point (a), is less immediately obvious. However, we can begin by first writing down the minimizer to the EIT problem about some reasonable initial guess σ_0 (in the least-squares sense)

$$\Delta\sigma = (H(\sigma_0) + \Gamma^{-1})^{-1} J(\sigma_0)^T (V_t - U(\sigma_0)) \quad (2)$$

where Γ is a given covariance matrix (specified in section 2.3) and V_t is a “true” measurement computed from the prescribed training data σ_t . We quickly observe that information on the the quality of EIT data generated from a specific electrode configuration is included in Eq. 2 via the forward model $U(\sigma_0)$, sensitivity matrix $J(\sigma_0)$, and the Hessian $H(\sigma_0)$ computed at σ_0 . In other words, Eq. 2 includes information on the data forward model and its 1st and 2nd derivatives. However, for this information to be usefully implemented in a training regime, we need to first write the full one-step Gauss-Newton estimate as

$$\hat{\sigma} = \sigma_0 + \Delta\sigma. \quad (3)$$

In this form, the information in Eq. 3 can then be directly included as a training input parameter by computing the misfit between the Gauss-Newton estimate and the true training data by taking the norm of their difference

$$\beta = \|\sigma_t - \hat{\sigma}\|^2. \quad (4)$$

It is worth noting that, while Eq. 4 does address the data quality requirement, it also directly includes information on the reconstruction quality by measuring the mismatch between reconstructed and true conductivities.

To summarize this subsection, we have derived two input parameters to drive training of the neural network detailed in the next section. These parameters, κ and β , include information on EIT data quality, ill-conditioning, and reconstruction quality – key variables needed to improve EIT imaging. Moreover, κ and β are both scalar quantities, containing a significant amount of information in a small amount of memory, which is a desirable feature when using them as training data for deep learning. Finally, when we concatenate

these parameters into an objective vector $\Theta = [\kappa, \beta]^T$, we surmise that an optimal electrode configuration has (theoretically) been attained when the following criterion is reached

$$\Theta = \begin{bmatrix} 1 \\ 0 \end{bmatrix}. \quad (5)$$

In practice, the condition number and data mismatch will always be greater than $\Theta = [1, 0]^T$; but, Eq. 5 can be used as a simple objective for the trained network described in the following subsection.

2.2. A deep learning-based algorithm for optimizing electrode positions

In the proposed approach, we aim to optimize 2D electrode configurations using trained deep neural networks. Generally speaking, deep learning aims to develop a mapping $Q : X \rightarrow Y$ between the elements of parameters X and Y [17]. In our approach, we aim to train a mapping to predict a vector of electrode locations E as a function of the objective vector Θ

$$E = Q_{\bar{\Theta}, \bar{E}}(\Theta) \quad (6)$$

using training data $\bar{\Theta}(\kappa, \beta) \in \mathbb{R}^{2 \times N_E N_\sigma}$ and randomized electrode positions $\bar{E} \in \mathbb{R}^{k \times N_E N_\sigma}$ consisting of $N_{\bar{E}}$ electrode configuration samples, N_σ conductivity samples, and k trial electrode midpoint coordinates¹. Given the generality of the approach outlined in Eq. 6, it was found that several practical constraints need to be prescribed to ensure a reliable $Q_{\bar{\Theta}, \bar{E}}$. Herein, we assume $Q_{\bar{\Theta}, \bar{E}}$ is only valid:

- For a fixed 2D geometry Ω .
- For a fixed k and homogeneous element width.
- When number of electrodes on a given side of Ω is fixed.
- When forward model function and method for computing J are fixed.
- When electrode contact impedances z are fixed.
- When the current injection I and measurement patterns M are fixed.
- When the maximum element size δ_e is fixed.

These constraints were adopted throughout this work and were determined after a preliminary error study using a suite of different neural networks and training data sizes/constitutions. From the preliminary study, we selected a feed forward neural network with two hidden layers. To compute the number of neurons per hidden layer, we used the fixed criteria described in [18] which proved robust in this application. To train $Q_{\bar{\Theta}, \bar{E}}$, we selected a regularized conjugate gradient backpropagation method with Fletcher-Reeves updates [19]. The performance of the training was evaluated using the mean squared error (MSE) and was stopped when either the MSE or the gradient were below 10^{-7} . This training architecture was chosen based on its speed (all examples trained in less than 5 minutes on a 8-core processor with 32 Gb RAM running computations in parallel in MATLAB) and ability to consistently produce physically realistic solutions (i.e. no overlapping electrodes and electrodes mapped outside of Ω).

For the purposes of visualization, a schematic illustration of a trained electrode position optimization network is shown in Fig. 1 where the number of optimized electrode positions is set to five. In the schematic, the input later (taking the objective vector Θ), the two hidden layers, and the output layer with five optimized electrode locations $E = [e_1, e_2, e_3, e_4, e_5]^T$ are shown.

2.3. Training, learning, and algorithm overview

The training data used in this work consists of two components: \bar{E} and $\bar{\Theta}$. \bar{E} is a matrix consisting of $N_{\bar{E}}$ different random electrode configurations subject to the constraints noted in the previous subsection. To generate different random electrode configurations, a vector of random electrode midpoint positions is input into the EIDORS [8] unstructured meshing routine. Following, the mesh generated using random electrode positions, prescribed current/measurement patterns, and conductivity samples are input into the numerical EIT forward model and sensitivity matrix function in order to compute $\bar{\Theta}$ parameters κ and β . Moreover, for each random electrode configuration, N_σ conductivity samples are utilized.

Importantly, the conductivity samples are computed only once to train $Q_{\bar{\Theta}, \bar{E}}$ and are reused in computing κ and β values for a given electrode configuration. The random conductivity samples tested herein are blob-line

¹Here, we converted the x, y midpoint coordinates to a single-column vector by simply stacking the x and y components (i.e. $[x, y] \rightarrow [x; y]$). Other approaches may also be useful, such as mapping the coordinates to a line corresponding to the perimeter.

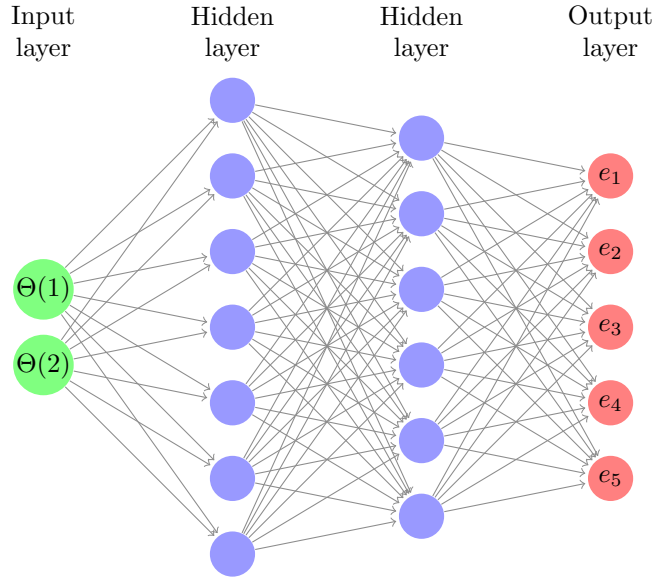


Figure 1: Schematic illustration of a trained electrode position optimization network where the number of optimized electrode positions is set to five. The input layer takes the optimization vector Θ , transfers this data to the two hidden layers, and outputs five optimized electrode locations $E = [e_1, e_2, e_3, e_4, e_5]^T$.

in structure and are drawn using the Cholesky factorization of the inverse covariance matrix (i.e. $L^T L = \Gamma^{-1}$) and the resulting generator $\bar{\sigma}_{\text{rand}} = L^{-1}r$, where r is a random non-negative vector. For completeness, Γ is a matrix determined element wise, where the entry (i, j) at locations x_i and x_j is given by

$$\Gamma(i, j) = a \exp \left(- \frac{\|x_i - x_j\|}{2b} \right) + c\delta_{ij} \quad (7)$$

where the scalars a , b , and c are positive and δ_{ij} is the Kronecker delta function. It should be noted that, since the meshing routine is unstructured, the number of elements and node locations vary slightly. As such, we simply interpolate the conductivity samples onto different meshes using linear interpolation.

Following the accumulation and storage of the training data, the data is fed into the training algorithm in order to learn the mapping $Q_{\Theta, E}$ using the general approach detailed in the previous subsection. One practical subtlety here is that regularization is required to ensure the network properly fits the data. In this work, we use L^2 regularization which necessitates the selection of a hyperparameter α . If α is too large, the network suffers from over fitting; on the other hand if α is too low, the system is poorly fit. For the problems addressed in this work $\alpha = 0.01$ was used. We remark that this is certainly not a globally optimal choice and the statistical selection of α will be addressed in future work. Another important assumption requiring elaboration is the selection of the “reasonable initial guess σ_0 .” For this, we chose the mean conductivity of a given sample. While a more accurate guess may be the best homogeneous estimate, the use of the mean value was found to be virtually indistinguishable from the best homogeneous estimate and saved significant computing time. To summarize the approach, training, and electrode position optimization approach proposed in this section, pseudocode is provided in Algorithm 1.

3. Examples and a metric for comparing the quality of electrode positioning

In this section we evaluate the proposed deep learning method for optimizing electrode positions considering three geometries: a square, a rectangle, and a triangle. While the former two geometries are rather common in engineering applications, the latter is used to test an irregular configuration. We begin by outlining a simple metric for determining the quality of electrode configurations, which will be used for comparison in the examples. Following, we demonstrate optimized electrode positions using the proposed algorithm.

3.1. Simple metric for determining the quality of electrode configurations

In order to numerically quantify (potential) improvements gained when using the optimized electrode position approach, we require a quality metric. While it is tempting to compare reconstructions of a similar target using a “standard” electrode configuration and an optimized one, this is not a reliable metric. This is because simulated data from an “electrode configuration A” may be significantly different in quality compared to “configuration B.” Therefore, if an optimized sensor configuration has higher quality simulated data than

Result: Obtain optimized electrode positions, E

initialize Ω , elwidth, k , δ_e , $N_{\bar{E}}$, N_σ , I , M , z , α ;

%% Generate training data \bar{E} and $\bar{\Theta}$ %%;

for $i = 1:N_{\bar{E}}$ **do**

 Generate random electrode positions, E^e ;

 Generate mesh from meshing routine: $\Omega^e = f(E^e, \Omega, \delta_e, \text{elwidth})$;

 Compute $\Gamma = \Gamma(\Omega^e)$;

if $i = 1$ **then**

 Generate N_σ random conductivity distributions using $\bar{\sigma}_{\text{rand}} = L^{-1}r$

end

for $j=1:N_\sigma$ **do**

if $j > 1$ **then**

 Interpolate conductivity sample to current mesh: $\bar{\sigma}_{\text{rand},j} \rightarrow \sigma_{\text{rand},j}$;

end

$V_t = U(\sigma_{\text{rand},j}, \Omega^e I, M, z)$ % “True” measurements;

$J = \frac{\partial U(\sigma_{\text{rand},j})}{\partial \sigma}$ % sensitivity matrix;

$H = J^T J$ % Hessian;

$\kappa = \|H^{-1}\| \|H\|$ % Condition number;

 %% 1-step Gauss-Newton estimate %%;

$\sigma_0 = \text{mean}(\sigma_{\text{rand},j})$ % Reasonable initial guess;

$J(\sigma_0) = f(\sigma_0)$ % sensitivity matrix about σ_0 ;

$H(\sigma_0) = J(\sigma_0)^T J(\sigma_0)$ % Hessian about σ_0 ;

$\Delta\sigma = (H(\sigma_0) + \Gamma^{-1})^{-1} J(\sigma_0)^T (V_t - U(\sigma_0))$ % Gauss-Newton update;

$\hat{\sigma} = \sigma_0 + \Delta\sigma$ % Gauss-Newton estimate;

$\beta = \|\sigma_t - \hat{\sigma}\|^2$ % Conductivity misfit;

 %% collect parameters%%;

$\theta(:, j) = [\kappa, \beta]^T$;

$\varepsilon(:, j) = E^e$;

end

$\bar{\Theta} = [\bar{\Theta}, \theta]$, $\bar{E} = [\bar{E}, \varepsilon]$;

end

%% Network training %%;

$L_1 = \text{floor}((k+2) \times N_{\bar{E}})^{1/2} + 2 \times (N_{\bar{E}}/(k+2))^{1/2}$ % Huang # neurons for layer 1;

$L_2 = \text{floor}(k \times (N_{\bar{E}}/(k+2))^{1/2})$ % Huang # neurons for layer 2;

$Q_{\bar{\Theta}, \bar{E}} = \text{train}(\bar{E}, \bar{\Theta}, L_1, L_2, \alpha)$ % CG backpropagation method with Fletcher-Reeves updates;

%% Compute optimized electrode positions, E %%;

$\Theta = [1, 0]^T$ % cf. Eq 5 text for rationale;

$E = Q_{\bar{\Theta}, \bar{E}}(\Theta)$ % Optimized electrode positions;

Algorithm 1: Pseudocode for generating training data \bar{E} and $\bar{\Theta}$, training the mapping $Q_{\bar{\Theta}, \bar{E}}$, and optimizing electrode positions.

a “standard” configuration, the potential quality of reconstructions is favorably biased towards the optimized configuration. In this sense, we require an “apples to apples” comparison.

To make such a comparison, let us first assume we are interested in determining the reliability of “electrode configuration A” (ECA). From a numerical perspective, ECA would be maximally reliable if ECA minimized the effects of discretization on computed voltages. Therefore, in a perfect world, the maximally reliable ECA would be able to simulate voltages from an infinitely large suite of conductivity samples – and compute the same voltages for each individual sample – using a coarse or a fine mesh. However, since all numerical models have error, we must quantify the reliability of electrode positioning statistically.

In order to do this, we take elements from the Bayesian approximation error approach (BAE) [20]. In BAE, the idea is to statistically model the error between an accurate model U_A and a reduced model U_h (generally represented by fine and coarse meshes). In the context of this work and determining the reliability of a given electrode configuration, we can also apply this methodology by first collecting the mean modeling error across N_σ conductivity samples

$$\mu = \frac{1}{N_\sigma} \sum_{j=1}^{N_\sigma} [U_A(\sigma_j) - U_h(\sigma_j)]. \quad (8)$$

Now, assuming we have collected ample conductivity samples and have two electrode configurations (A and B) with resulting mean modeling errors μ_A and μ_B : we can confidently state that “electrode configuration A” is more reliable than “electrode configuration B” when the overall magnitude of μ_A is significantly lower than μ_B . This statement can be put more plainly as, the use of “electrode configuration A” results less statistical modeling error than “electrode configuration B” when $\|\mu_A\|_1 < \|\mu_B\|_1$.

The advantage of using this metric for quantifying the quality of electrode configurations is that it is independent from the metrics used to optimize the electrode configurations. As such, the comparison of mean modeling errors for different electrode configurations (optimized and “standard” layouts) using fine and coarse meshes will be used in the examples for the purpose of quantitative comparison.

3.2. Example parameters

For these examples demonstrated herein, we assume the maximum element size used in training is equal to the fixed electrode width, the minimum training element size is half the fixed electrode width, contact impedances $z = 10^{-5}$, 1 mA current injections ($k - 1$ injections against electrode 1), and $k(k - 1)$ adjacent electrode measurements. The units of length and conductivity in all examples are cm and mS/cm, respectively. To train the mapping $Q_{\bar{\Theta}, \bar{E}}$, $N_{\bar{E}} = 200$ electrode configuration samples and $N_\sigma = 200$ conductivity samples are drawn per example geometry.

In order to quantify the quality of optimized electrode configurations, coarse and fine meshes will be generated using (i) the optimized electrode positions and (ii) one “standard” electrode configuration (i.e. uniform spacing of electrodes along the geometry edges). The coarse meshes will have the same maximum element size used in training and the fine meshes will have a maximum element size half of these values. Following, Eq. 8 will be used as the statistical metric for comparative quality evaluation.

3.3. Example 1: 1×1 square

In this example, we examine the optimized electrode configuration generated for a 1×1 unit square having $k = 12$ electrodes. The geometry was prescribed three electrodes per side with a fixed electrode width of 0.075. To illustrate the example graphically, one random conductivity draw and two random electrode configurations are shown in Fig. 2 (electrodes shown in green). Note the counterclockwise ascending numbering of electrodes starting from the top right-hand corner of the geometry (consistent numbering is maintained through the paper).

After generating the training data, the neural network was trained following the procedure highlighted in the previous section. Representative plots taken after the completion of training are provided in Fig. 3, where the MSE performance and gradient drops are both provided throughout the training epochs. The total time required to train the model $Q_{\bar{\Theta}, \bar{E}}$ was approximately two minutes over a total of 909 epochs. This performance was similar among all examples studied in this work.

Upon training $Q_{\bar{\Theta}, \bar{E}}$, the optimized electrode configuration was computed by inputting $\Theta = [1, 0]^T$ into $Q_{\bar{\Theta}, \bar{E}}$. The optimized configuration is shown in Fig. 4(a). On first glance, it appears that the optimized electrode locations do not vary significantly in comparison to the uniform electrode layout shown in Fig. 4(b). However, to investigate this closer, we plot the uniform layout atop the optimized layout, as shown in Fig. 4(c). In Fig. 4(c), we can clearly see notable differences between the uniform and optimized positions; we also observe that the optimized electrode positions are close to, but not exactly evenly spaced. These small perturbations in the optimized positions appear to be random and are roughly 0.05 in magnitude. The perturbations can be viewed as errors since, from the symmetry of the geometry, optimized electrode spacing should be uniform – whereas, e.g., electrode 1 is clearly too close to electrode 2. The source of errors likely results from over-fitting and/or

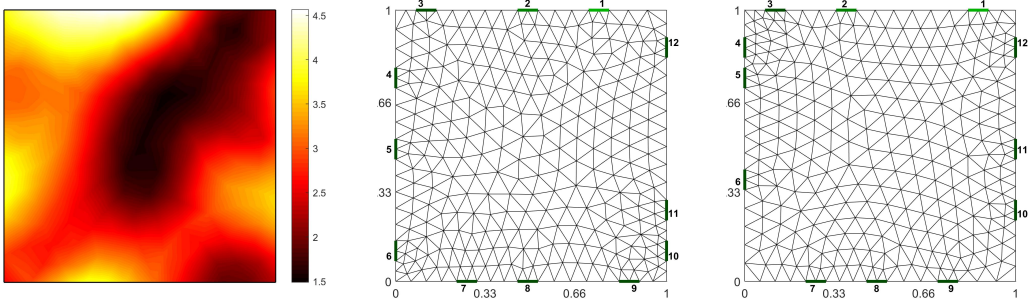


Figure 2: Left column: one random conductivity draw from the training data (units, mS/cm). Middle column and right columns: randomized electrode locations taken from the training data. Electrode locations are indicated numerically and are organized as counterclockwise ascending from the top right-hand corner of the geometry.

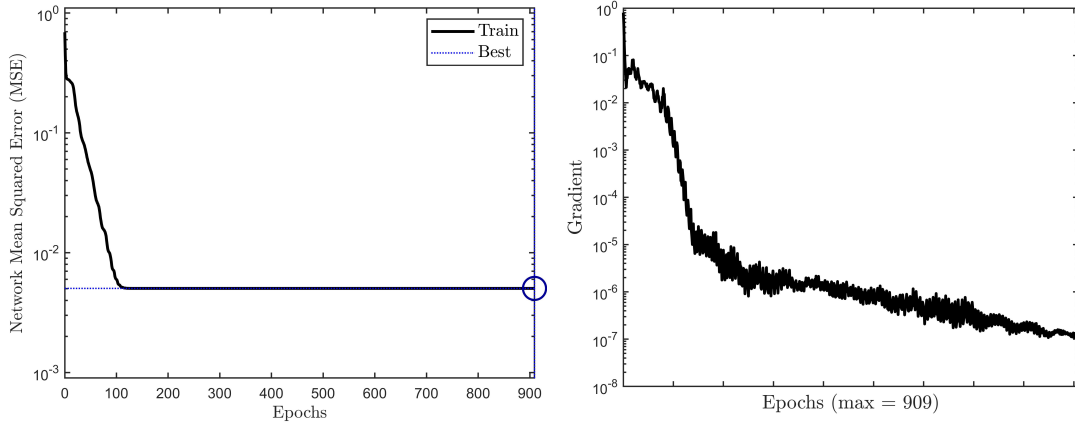


Figure 3: Training plots for the network $Q_{\Theta, \bar{E}}$. The left-hand side shows the MSE performance while the right-hand side shows the gradient drops across the training epochs.

the distance from the objective vector Θ to the fitted data (i.e. $\Theta = [1, 0]^T$ is too far from the trained values of κ and β). At this point, a comparison of the optimized and uniform electrode configurations' quality would be useful to determine the optimization approach's effectiveness. This comparison, showing the mean modeling errors for N_σ samples using coarse and fine meshes shown in Fig 4(a,b), is provided in Fig. 5.

The results of the electrode positioning quality analysis, shown in Fig. 5, are highly unexpected. The use of optimized electrode positioning resulted in a drastic reduction in mean modeling errors compared to the "standard" uniform layout. In fact, the cumulative sum of mean errors for the uniform layout $\|\mu_S\|_1$ was approximately 18 times higher than the cumulative sum of mean errors for the optimized layout $\|\mu_O\|_1$, i.e. $\|\mu_S\|_1/\|\mu_O\|_1 \approx 18$. This indicates that, despite the small electrode positioning differences between the optimized and "standard" uniform layout, the electrode position optimization approach was highly effective. Moreover, this result demonstrates the ill-conditioned nature of the electrode positioning problem – i.e., small changes in electrode positions result in large changes in modeling errors.

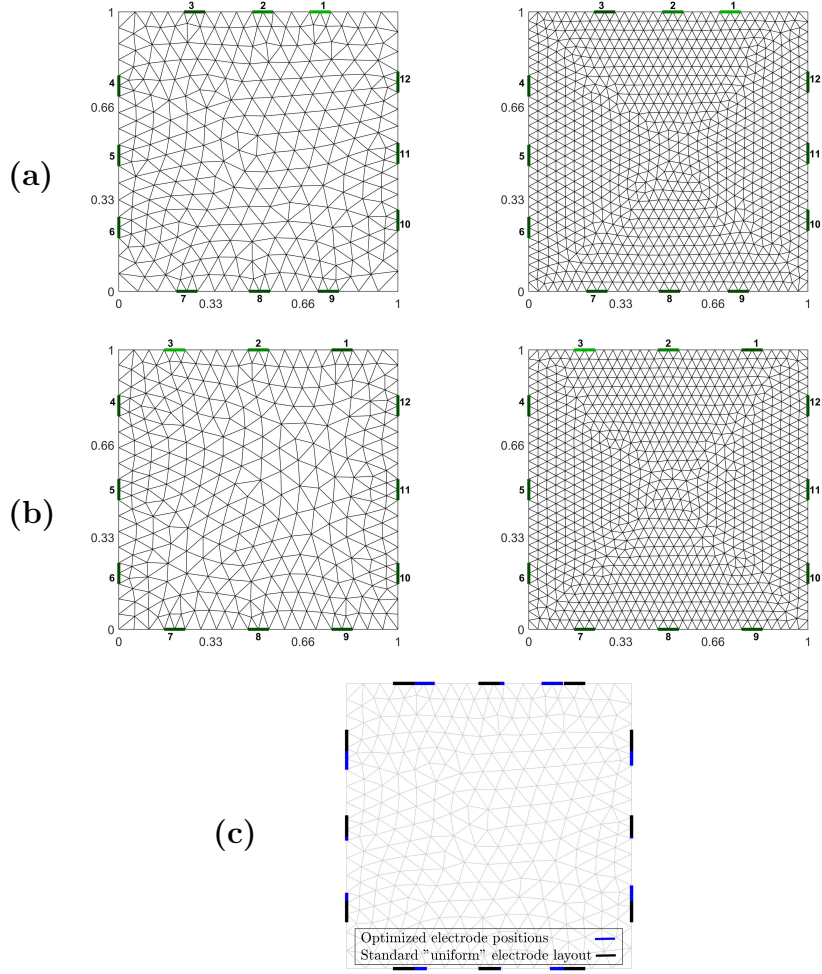


Figure 4: 1×1 meshes for the (a) optimized electrode positions and (b) “standard” (evenly-spaced) electrode positions and (c) an overlay comparing the uniform electrode positions (black) plotted atop the optimized electrode positions (blue). Coarse and fine meshes used in the quality analysis are shown on the left- and right-hand sides, respectively.

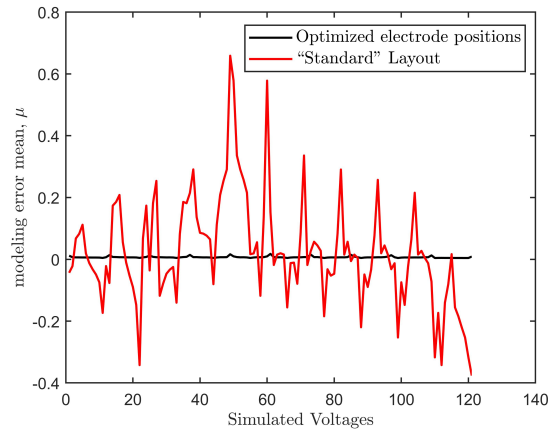


Figure 5: Comparison of quality metrics μ for the optimized electrode positions (black) and “standard” positions (red) for the 1×1 example.

3.4. Example 2: 2×1 rectangle

In this example, we study a 2×1 rectangle and again consider $k = 12$ electrodes. However, in this example, we assume the short sides have 2 electrodes, whereas the longer sides have 4 electrodes. We have followed the same procedure discussed in the previous subsection and for the purposes of conciseness and to avoid repetition, we immediately show the optimized electrode configuration in Fig. 6(a). The comparative uniformly-spaced “standard” layout with electrodes located at the one fifth and one third points on the long and short sides, respectively, is shown in Fig. 6(b). The differences in electrode positions are shown in Fig. 6(c) for direct comparison.

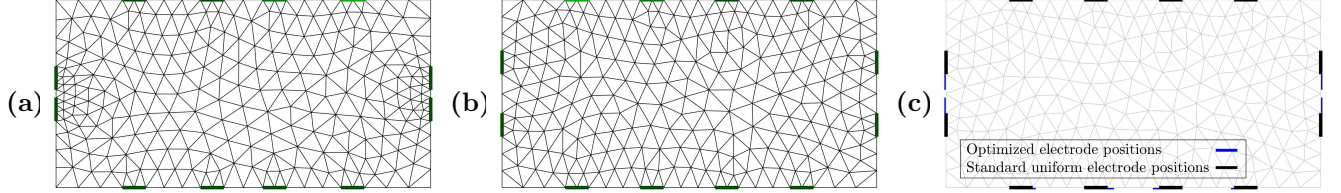


Figure 6: 2×1 coarse meshes for the (a) optimized electrode positions and (b) “standard” (evenly-spaced) electrode positions and (c) an overlay comparing the uniform electrode positions (black) plotted atop the optimized electrode positions (blue).

Upon immediate visual inspection and comparison of the optimized and “standard” electrode positions shown in Fig. 6(a,b), the largest visual difference is the placing of the short-side electrodes (since the central coordinates of the top and bottom side electrode differ by a maximum of ≈ 0.10 cm). This is confirmed in the electrode position discrepancy plot in Fig. 6(c). On first thought, one may hypothesize that the number of elements differ significantly between the two configurations, which – in itself – may drive significant differences in the finite element matrix condition numbers. However, the meshes vary by only approximately 20 nodes/elements, so the effect of element/node number is marginal. As such, the locations of the electrodes on the short sides must play a major role in the optimality of the mesh in Fig. 6(a). Therefore, for this geometry, the movement of the end electrodes towards each other functions to increase the information in EIT data and reduce the ill-conditioning the and Hessian matrices – one possible mechanism for this is likely the increasing distance between current injections. Using N_σ different trial conductivity samples, we found, on average, a reduction of 5 – 14% in the 2-norm condition numbers of the optimized configuration’s Hessian matrices compared to the uniform configuration – which confirms the former hypothesis regarding the end electrode locations.

What remains in this analysis is a quantification of the optimized electrode configuration quality in comparison to the uniform layout, which is shown in Fig. 7. A similar trend observed in the square example is also observed here. In this example, the uniform layout mean error $\|\mu_S\|_1$ was approximately 30 times higher than the cumulative sum of mean errors for the optimized layout $\|\mu_O\|_1$, i.e. $\|\mu_S\|_1/\|\mu_O\|_1 \approx 30$. This improvement in modeling error again confirms the effectiveness of the optimization approach. Interestingly, we found a greater reduction in the mean error using optimized electrode positions in this example relative to the square example. This may indicate that the use of optimized electrode configurations in slender geometries has a greater impact on the quality of EIT reconstructions than in geometries with an aspect ratio approaching 1 to 1. This realization is intuitively logical since the optimal electrode configurations – at least for randomized or homogeneous conductivity distributions – for square or circular geometries are (or nearly are) uniform, as demonstrated in the previous example and also inferred from symmetry.

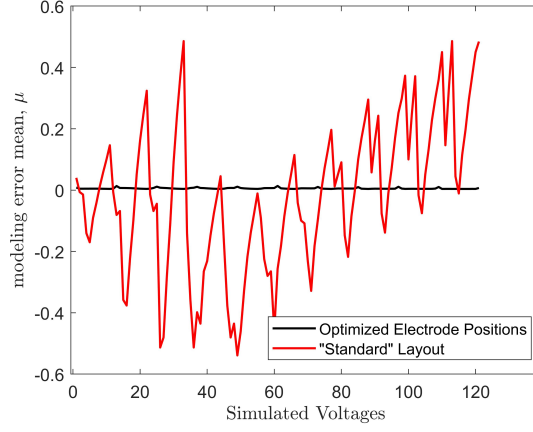


Figure 7: Comparison of quality metrics μ for the optimized electrode positions (black) and “standard” positions (red) for the 2x1 example.

3.5. Example 3: 1x1 triangle

This example explores electrode position optimization for a 1x1 triangle. Here, we assume that the hypotenuse has 4 electrodes and the other sides have three electrodes, for a total of $k = 10$ electrodes. The uniform control electrode configuration used for comparison has electrode midpoints located at one fifth points along all sides. The optimized, uniform control, and comparative electrode configurations are shown in Fig. 8.

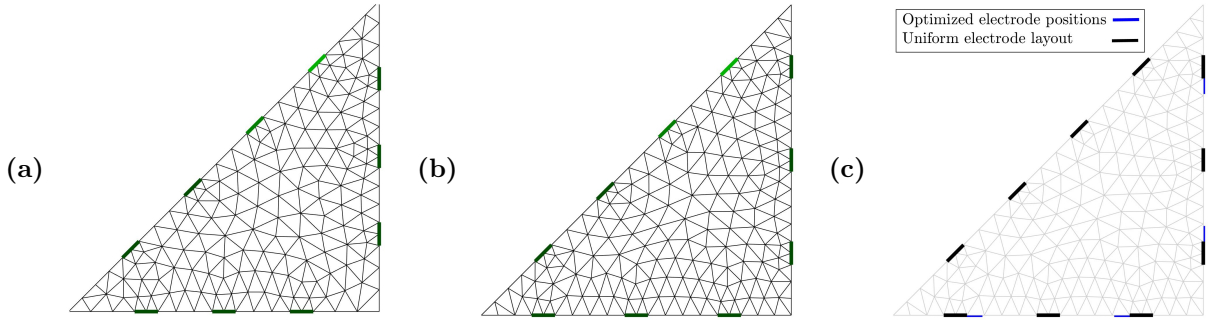


Figure 8: 1x1 triangle geometry coarse meshes for the (a) optimized electrode positions and (b) “standard” (evenly-spaced) electrode positions and (c) an overlay comparing the uniform electrode positions (black) plotted atop the optimized electrode positions (blue).

We immediately notice that the optimized electrode positions on the diagonal match nearly exactly with those on the control triangle. On the bottom and right-hand sides, we observe that the middle optimized electrode positions are the same as the control, while the others are slightly different. In fact, the optimized electrodes on the bottom and right-hand sides are located at one quarter, one half, and three quarters the side length within a precision of 0.01. Given the small differences, it would be interesting to determine if the resulting modeling errors for each configuration also vary by only a small amount. To investigate this, the mean error plots for both electrode configurations are shown in Fig. 9.

In this case, we clearly see that the mean errors of the optimized electrode positions are only slightly lower than the errors from the control triangle. For this example, the cumulative ratio of the electrode quality metrics is $\|\mu_S\|_1 / \|\mu_O\|_1 \approx 1.07$. In other words, the optimized configuration only outperformed the control configuration by approximately 7% – which again supports the effectiveness of the optimization approach, albeit the improvement is small. However, this is an interesting observation, which indicates that unlike the square and rectangular examples, EIT forward models for triangular geometries are less sensitive to perturbations in electrode positions. Intuitively, this result makes sense since the electric current is much more concentrated towards the center in the triangle. Therefore, small changes in the electrode position do not affect the electric fields as drastically as in the previous examples. We can therefore conclude that the effectiveness of the optimization regime is significantly influenced the target geometry.

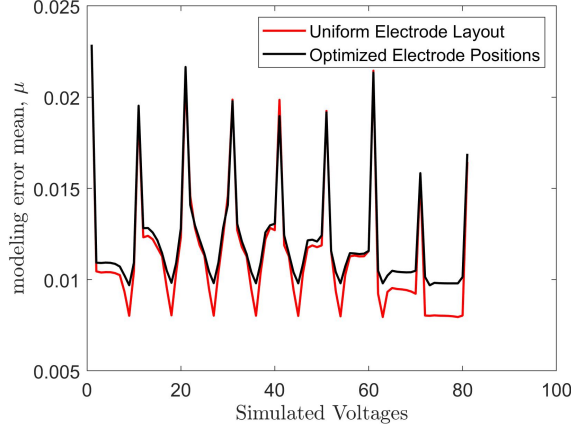


Figure 9: Comparison of quality metrics μ for the optimized electrode positions (black) and uniform control positions (red) for the triangular geometry.

4. Discussion: curious geometries, current limitations, and future work

To this point, this article has investigated rather simple geometries and shown the effectiveness of the deep learning based approach for optimizing electrode configurations for these cases. But, can the algorithm handle more complex geometries and to what extent is the optimization approach still viable?

We began by investigating this query by considering rectangular cases where the aspect ratio $\gamma = \frac{\text{width}}{\text{height}}$ is large and found the deep learning approach highly sensitive to the value of the regularization parameter for $\gamma \gtrsim 10$ due to the large amount of possible electrode location possibilities along the geometry’s width. Generally speaking, however, the number of electrode position possibilities truly stems from (a) the ratio of the perimeter to homogeneous element width and (b) the minimum/maximum element size. In addition to this, when the aspect ratio becomes arbitrarily large and the geometry’s height is arbitrarily small, the physics of the problem breaks down since the 2D geometry approaches a line. Nonetheless, sensible optimized solutions are still attained up to around $\gamma = 8$ using the same regularization parameter adopted throughout this work – an example for $\gamma = 8$ is shown in Fig. 10(a).

It is intuitively interesting to investigate optimal solutions for complex geometries, in particular those with geometrical discontinuities. Take for example a square geometry with $k = 16$ electrodes and an equilateral triangular hole in the center as shown in Fig. 10(b). Obviously, when the length of triangle’s bottom side is equal to the square’s width, we develop a circuit short in the current injection protocol and electrode measurements are meaningless. On the other hand, when the triangle is arbitrarily small, the optimized electrode positions are the same as the unaltered square geometry. But, optimized solutions for the intermediate range are certainly worth inquiry and are shown Fig. 10(b,c). Comparing the optimized positions in the triangular hole examples, we notice that the only significant difference in the electrode positions is a downward shift in the furthestmost bottom side electrodes, which provides compensating information when the bottom side of the triangle approaches the square sides. All in all, it is a bit counter-intuitive that such a large change in the hole size resulted in only a small change in the optimized positions – on the other hand, the EIT forward model has a low sensitivity to changes far from the boundary.

Continuing this train of thought, we examine another square geometry with $k = 12$ electrodes where a square hole is placed near the top left corner boundary. We observe the optimized configuration for this geometry in Fig. 10(d) and note that the electrodes on the top and left sides are localized near the hole, while the opposite side electrodes are spaced rather uniformly. This configuration is consistent with the previous statement regarding the sensitivity of the EIT forward model and demonstrates the tendency of electrodes to localize near non-conductive objects close to the boundary in optimized configurations.

The former example also begins to illuminate the effects of partial domain segmentation (i.e., splitting of different regions in the geometry). Indeed, one could deduce that the L-shape in the top left-hand corner is locally segmented from the rest of the domain and that EIT information is improved when electrodes are localized near the segmented area. However, what if the entire square domain is partially segmented? We investigate this query in Fig. 10(e) and immediately notice that the top and bottom side electrodes in the optimal configuration have again localized near the rectangular hole approaching the top and bottom boundary while the left and right sides, far from the hole, are roughly uniformly spaced. This result again demonstrates that near-boundary effects have a large impact on the local positioning of the optimized electrodes and a small effect on electrodes far away.

What remains to be discussed is the effects of over-fitting and regularization of the neural network, elements which are closely related. We noted that a constant regularization term was used throughout this work, which

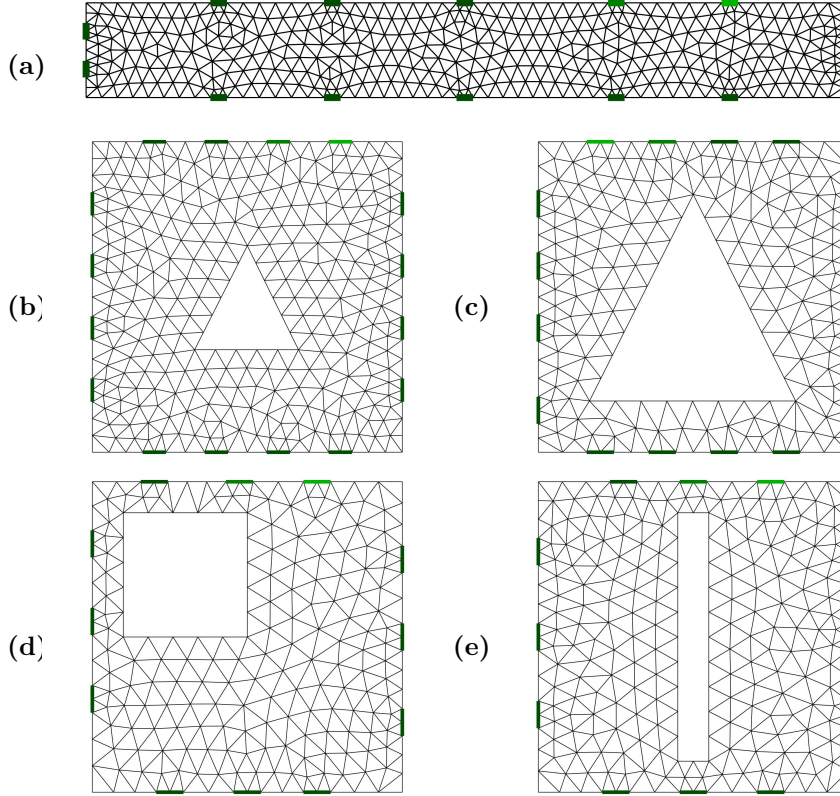


Figure 10: Examples of optimized electrode positions using the deep learning based approach for various geometries.

was shown to be reasonably robust but certainly not optimal for every optimization problem. The effects of this were not pronounced in the examples provided and were mainly manifested in small (seemingly random) perturbations in optimized electrode positions. This was most obvious in Fig 4(a), where the electrode spacings were not completely symmetric as expected. Of course, the type and amount of training data also plays a role here; however, tailored changes in the regularization parameter for a given problem did fix this issue in preliminary trials, indicating that the choice of the regularization parameter had the most significant effect for the problems considered herein.

In future work, we look forward to improving the robustness of the deep learning approach to electrode position optimization. Some remaining challenges to address are centered around mitigating the effects of over-fitting and improving the robustness to a broader range of conductivity distributions (such as non-conductive cracks for non-destructive testing purposes). For this, we look forward to integrating Bayesian regularized convolutional neural networks [21], taking advantage of automatic regularization and the use of conductivity distributions in the training data. In addition, we anticipate the inclusion of internal electrodes into the optimization approach to improve the sensitivity of EIT to inclusions far from the boundary.

5. Conclusions

In this article, we proposed a straightforward deep learning based approach for optimizing electrode positions used in EIT sensing. To evaluate the quality of the optimized electrode configurations, a simple statistical metric was developed and applied to compare optimized configurations with “standard” uniformly distributed electrode layouts. The effectiveness of the optimization approach was demonstrated in a suite of examples, where reductions in cumulative modeling error up to a factor of 30 were observed when employing optimized electrode positions relative to the “standard” configurations. In the analysis, it was found that the following items notably influenced the solutions from of the optimization approach (in no particular order):

- The aspect ratio of the target geometry (if rectangular).
- The regularization parameter used in training the neural network.
- Localized domain segmentation.
- Near-boundary effects (such as holes).
- The condition number of the finite element stiffness matrix.

Moreover, in future work, we aim to address robustness issues related to over-fitting and regularization of the neural network. To do this, we aim to include a Bayesian regularized convolutional neural network in order to take advantage of automatic regularization and the inclusion of conductivity distributions directly in the training data. These frameworks will be extended to include internal electrodes to improve the sensitivity of EIT to inclusions far from the boundary.

Acknowledgments

DS would like to acknowledge the support of the Department of Civil and Structural Engineering at the University of Sheffield. DL was supported by the National Natural Science Foundation of China under Grant No. 61871356.

References

- [1] H. Hassan, T. N. Tallman, Failure prediction in self-sensing nanocomposites via genetic algorithm-enabled piezoresistive inversion, *Structural Health Monitoring* (2019) (in press).
- [2] T. N. Tallman, K. Wang, Damage and strain identification in multifunctional materials via electrical impedance tomography with constrained sine wave solutions, *Structural Health Monitoring* 15 (2) (2016) 235–244.
- [3] T. Tallman, S. Gungor, G. Koo, C. Bakis, On the inverse determination of displacements, strains, and stresses in a carbon nanofiber/polyurethane nanocomposite from conductivity data obtained via electrical impedance tomography, *Journal of Intelligent Material Systems and Structures* (2017) 1–13.
- [4] K. J. Loh, T.-C. Hou, J. P. Lynch, N. A. Kotov, Carbon nanotube sensing skins for spatial strain and impact damage identification, *Journal of Nondestructive Evaluation* 28 (1) (2009) 9–25.
- [5] D. Smyl, S. Bossuyt, W. Ahmad, A. Vavilov, D. Liu, An overview of 38 least squares-based frameworks for structural damage tomography, *Structural Health Monitoring* (2019) 1475921719841012.
- [6] D. Smyl, M. Pour-Ghaz, A. Seppänen, Detection and reconstruction of complex structural cracking patterns with electrical imaging, *NDT & E International* 99 (2018) 123–133.
- [7] A. Seppänen, A. Voutilainen, J. Kaipio, State estimation in process tomographyreconstruction of velocity fields using eit, *Inverse Problems* 25 (8) (2009) 085009.
- [8] A. Adler, W. R. Lionheart, Uses and abuses of eiders: an extensible software base for eit, *Physiological measurement* 27 (5) (2006) S25.
- [9] J. L. Mueller, S. Siltanen, *Linear and nonlinear inverse problems with practical applications*, SIAM, 2012.
- [10] J. Kaipio, A. Seppänen, E. Somersalo, H. Haario, Posterior covariance related optimal current patterns in electrical impedance tomography, *Inverse Problems* 20 (3) (2004) 919.
- [11] W. R. Lionheart, J. Kaipio, C. N. McLeod, Generalized optimal current patterns and electrical safety in eit, *Physiological measurement* 22 (1) (2001) 85.
- [12] N. Polydorides, H. McCann, Electrode configurations for improved spatial resolution in electrical impedance tomography, *Measurement Science and Technology* 13 (12) (2002) 1862.
- [13] N. Hyvonen, A. Seppanen, S. Staboulis, Optimizing electrode positions in electrical impedance tomography, *SIAM Journal on Applied Mathematics* 74 (6) (2014) 1831–1851.
- [14] L. Horesh, E. Haber, L. Tenorio, Optimal experimental design for the large-scale nonlinear ill-posed problem of impedance imaging, *Large-Scale Inverse Problems and Quantification of Uncertainty* (2010) 273–290.
- [15] P. Vauhkonen, M. Vauhkonen, T. Savolainen, J. Kaipio, Three-dimensional electrical impedance tomography based on the complete electrode model, *IEEE T. Biomedical Eng.* 46 (9) (1999) 1150–1160.
- [16] D. Smyl, D. Liu, Less is often more: Applied inverse problems using hp-forward models, *Journal of Computational Physics* (2019) 108949.
- [17] S. Arridge, A. Hauptmann, Networks for nonlinear diffusion problems in imaging, *arXiv preprint arXiv:1811.12084*.

- [18] G.-B. Huang, Learning capability and storage capacity of two-hidden-layer feedforward networks, *IEEE Transactions on Neural Networks* 14 (2) (2003) 274–281.
- [19] N. M. Nawi, R. Ransing, M. Ransing, An improved conjugate gradient based learning algorithm for back propagation neural networks, *International Journal of Computational Intelligence* 4 (1) (2007) 46–55.
- [20] A. Nissinen, L. Heikkinen, J. Kaipio, The bayesian approximation error approach for electrical impedance tomographyexperimental results, *Measurement Science and Technology* 19 (1) (2007) 015501.
- [21] J. Snoek, O. Rippel, K. Swersky, R. Kiros, N. Satish, N. Sundaram, M. Patwary, M. Prabhat, R. Adams, Scalable bayesian optimization using deep neural networks, in: *International conference on machine learning*, 2015, pp. 2171–2180.